



Cite this: *Mater. Adv.*, 2020, **1**, 54

## FeNiMo trimetallic nanoparticles encapsulated in carbon cages as efficient hydrogen evolution reaction electrocatalysts†

Ziqi Zhang,<sup>a</sup> Linchuan Cong,<sup>a</sup> Zhuochen Yu,<sup>a</sup> Lina Qu,<sup>a</sup> Miaomiao Qian<sup>a</sup> and Weimin Huang  <sup>a,b</sup>

Hydrogen is one of the most desirable alternatives to fossil fuels due to its renewability and large energy density. The electrocatalytic hydrogen evolution reaction (HER) is drawing more and more attention since it can produce H<sub>2</sub> powered by renewable energy. Therefore, efficient and durable electrocatalysts are an urgent need. On the one hand, the high price and low reserve of noble metals hinder their further applications. On the other hand, various non-noble metal electrocatalysts cannot achieve satisfactory stability and efficiency. Thus, this paper reports a cheap and feasible way to synthesize a carbon cage-encapsulated FeNiMo compound. It exhibits the desired overpotentials of 199 mV at 10 mA cm<sup>-2</sup> in an alkaline solution and 246 mV at 10 mA cm<sup>-2</sup> in an acidic solution. Besides, it exhibits similar current density loss to commercial Pt/C after 10 000 CV cycles, which suggests satisfactory durability.

Received 2nd March 2020,  
Accepted 10th March 2020

DOI: 10.1039/d0ma00065e

rsc.li/materials-advances

### 1. Introduction

The increasing greenhouse effect has aroused increasing attention towards renewable energy source conversion and storage.<sup>1</sup> Hydrogen is considered as one of the most desirable alternatives to fossil fuels.<sup>2</sup> The electrocatalytic hydrogen evolution reaction (HER) can produce H<sub>2</sub> powered by renewable energy, including solar or wind energy.<sup>3,4</sup> In order to drive HER with a lower overpotential, efficient and durable electrocatalysts are an urgent need.<sup>5</sup> Although noble metals such as Pt, Ir and Ru are used as mainstream electrocatalysts, their high cost and low abundance hinder their further applications.<sup>6</sup> Therefore, the use of low-cost and earth-abundant electrocatalysts to replace noble metal catalysts is necessary.<sup>7–9</sup> Recently, many transition metals and their compounds have been used as non-noble electrocatalysts, including transition metal oxides,<sup>10</sup> sulfides,<sup>11–14</sup> phosphides,<sup>15–20</sup> carbides,<sup>21</sup> and nitrides.<sup>22</sup> Among them, the compounds based on Co, Fe and Ni are most frequently used as electrocatalysts for HER due to their low cost and deficient 3d electron structures.<sup>23–25</sup> However, due to their weak electronic conductivity and stability, the electrocatalysts based on Fe, Ni and Co are still not able to compete with noble-metal-based

electrocatalysts.<sup>26</sup> Therefore, we aim to solve these issues in two ways. First, we can establish unique carbon nanostructures, such as carbon nanotubes<sup>27</sup> and graphene,<sup>28</sup> to enhance the conductivity and stability morphologically. Second, we can combine the metals (Mo) on the left half of the transition metals in the periodic table with the metals (Fe and Ni) on the right half of the series with more filled d-bands, which can build well-pronounced synergism in electrocatalysis.<sup>29</sup>

In this paper, we report a new Fe, Ni and Mo trimetallic compound encapsulated in a carbon cage as an efficient HER electrocatalyst. This material was synthesized by a two-step hydrothermal reaction at room temperature and one-step direct carbonization, which is facile, low-cost and environmentally friendly. It exhibits the desired overpotentials of 199 mV at 10 mA cm<sup>-2</sup> in an alkaline solution and 246 mV at 10 mA cm<sup>-2</sup> in an acidic solution. Besides, it has satisfactory durability, which is better than that of a commercial Pt/C catalyst.

### 2. Experimental section

#### 2.1. Reagents

Potassium ferricyanide (K<sub>3</sub>[Fe(CN)<sub>6</sub>], analytical reagent), potassium ferrocyanide trihydrate (K<sub>4</sub>[Fe(CN)<sub>6</sub>]<sub>3</sub>·3H<sub>2</sub>O, analytical reagent), sodium citrate (Na<sub>3</sub>C<sub>6</sub>H<sub>5</sub>O<sub>7</sub>, 99%), ethyl alcohol (C<sub>2</sub>H<sub>5</sub>OH, ≥99.8%), sulfuric acid (H<sub>2</sub>SO<sub>4</sub>, 98%) and potassium hydroxide (KOH, 96%) were obtained from Beijing Chemical Works. Nickel nitrate hexahydrate (Ni(NO<sub>3</sub>)<sub>2</sub>·6H<sub>2</sub>O, 98%) and ammonium molybdate tetrahydrate (H<sub>24</sub>Mo<sub>7</sub>N<sub>6</sub>O<sub>24</sub>·4H<sub>2</sub>O) were

<sup>a</sup> College of Chemistry, Jilin University, Changchun 130012, China.

E-mail: huangwm@jlu.edu.cn; Tel: +86-431-80561579

<sup>b</sup> Key Laboratory of Physics and Technology for Advanced Batteries of Ministry of Education, Jilin University, Changchun 130012, China

† Electronic supplementary information (ESI) available. See DOI: 10.1039/d0ma00065e



obtained from Aladdin. Pt/C (20 wt%, JM), Nafion (5.0 wt%, Dupont), and N<sub>2</sub> gas (99.99%) were also employed. All chemical reagents were used as received without further purification. All aqueous solutions were prepared with ultrapure water (resistivity of 18.25 MΩ cm).

## 2.2. Physical characterization

Scanning electron microscopy (SEM) was performed on a HITACHI SU020 microscope. Transmission electron microscopy (TEM) and elemental mapping were performed on an FEI Tecnai G20/JEM2010 microscope. X-ray photoelectron spectra (XPS) were recorded on a Thermo ESCALAB 250Xi with an excitation source of Al K $\alpha$  radiation. X-ray diffraction (XRD) patterns were carried out using an Empyrean (PANalytical B.V.) with a Cu K $\alpha$  radiation source ( $\lambda_1 = 1.5406$  Å) operating at 40.0 kV and 40.0 mA, and the diffraction data were recorded in the 2 $\theta$  range of 5–80° with a scan rate of 4 degrees per min.

## 2.3. Preparation of Fe<sup>3+</sup>NiMoC

In a typical procedure,<sup>30</sup> 0.6 mmol of nickel nitrate and 0.9 mmol of sodium citrate were dissolved in 20 mL of deionized (DI) water to form solution A, and 0.4 mmol of potassium ferricyanide was dissolved in another 20 mL of DI water to form solution B. Solutions A and B were then mixed under stirring for 1 min. The obtained mixed solution was aged for 18 h at room temperature. The mixed solution was centrifuged and washed several times with DI water and dried in a vacuum overnight at 60 °C to obtain the Fe–Ni Prussian blue analogue (Fe<sup>3+</sup>Ni-PBA). In addition, 0.4 mmol of ferrocyanide trihydrate was used to take the place of 0.4 mmol of potassium ferricyanide and the product was named Fe<sup>2+</sup>Ni-PBA.

Next, 200 mg of Fe<sup>3+</sup>Ni-PBA was dissolved in 10 ml of DI water, which was subsequently injected into 10 ml of DI water containing 200 mg of ammonium molybdate tetrahydrate. The mixed solution was then stirred for 24 h at room temperature, centrifuged with DI water several times and dried overnight in a vacuum at 60 °C to get Fe, Ni and Mo compounds named Fe<sup>3+</sup>NiMo. In addition, Fe<sup>2+</sup>Ni-PBA was treated in the same way to get Fe<sup>2+</sup>NiMo. The precipitate (Fe<sup>2+</sup>NiMo or Fe<sup>3+</sup>NiMo) was heated at 800 °C for 4 h at a rate of 3 °C min<sup>-1</sup> in a tube furnace and in N<sub>2</sub> atmosphere to obtain the carbide of FeNiMo compounds. The final products were named Fe<sup>3+</sup>NiMoC or Fe<sup>2+</sup>NiMoC, respectively. As control groups, Fe<sup>2+</sup>Ni-PBA and Fe<sup>3+</sup>Ni-PBA were heated under the same conditions as above to get the corresponding carbonization products, which were named Fe<sup>2+</sup>Ni-PBAC and Fe<sup>3+</sup>Ni-PBAC, respectively.

## 2.4. Cathode preparation

Briefly, 5 mg of (Fe<sup>2+</sup>Ni-PBAC, Fe<sup>3+</sup>Ni-PBAC, Fe<sup>2+</sup>NiMoC, Fe<sup>3+</sup>NiMoC or Pt/C (20 wt%)) was dispersed in 240 μL of a mixed solution of ethyl alcohol, 240 μL of ultrapure water and 20 μL of 5 wt% Nafion and ultrasonicated for 10 min. Next, 5 μL of liquid was pipetted onto the surface of a glassy carbon electrode (GCE, 3 mm) (loading ~0.7077 mg cm<sup>-2</sup>) and allowed to dry naturally. The modified GCE served as the working electrode.

## 2.5. Electrochemical measurements

Electrochemical measurements were performed using a CHI 660E electrochemical workstation with a three-electrode system that included a working electrode (GCE), a counter electrode (Pt foil, 1 × 1 cm<sup>2</sup>) and a reference electrode (Hg/HgO, 1 M KOH electrolyte) in 1 M KOH solution, or a Hg/Hg<sub>2</sub>SO<sub>4</sub> (saturated K<sub>2</sub>SO<sub>4</sub> electrolyte) electrode in 0.5 M H<sub>2</sub>SO<sub>4</sub> solution. The experimental potential values were calibrated by using the following equation:  $E$  vs. RHE =  $E$  vs. Hg/HgO + 0.098 + 0.059 pH;  $E$  vs. RHE =  $E$  vs. Hg/Hg<sub>2</sub>SO<sub>4</sub> + 0.616 + 0.059 pH. Before the test, N<sub>2</sub> flow (20 mL min<sup>-1</sup>) was continuously fed to the cathode through the electrolyte in the cell for 30 min. The linear sweep voltammetry (LSV) experiments were performed at a scan rate of 10 mV s<sup>-1</sup> from 0.2 to -0.7 V (vs. RHE) in N<sub>2</sub>-saturated 0.5 M H<sub>2</sub>SO<sub>4</sub> or 1 M KOH solution, respectively. Electrochemical impedance spectra (EIS) measurements were performed at an overpotential of 300 mV (vs. RHE) with frequencies from 0.1 to 100 000 Hz and an amplitude of 5 mV. The electrochemically active surface area (ECSA) was estimated by CVs and was tested from -0.80 to -0.70 V (vs. Hg/HgO) with a scan rate from 10 to 100 mV s<sup>-1</sup> in N<sub>2</sub>-saturated 1 M KOH, or tested from -0.65 to -0.55 V (vs. Hg/Hg<sub>2</sub>SO<sub>4</sub>) with a scan rate from 10 to 100 mV s<sup>-1</sup> in N<sub>2</sub>-saturated 0.5 M H<sub>2</sub>SO<sub>4</sub>. Durability cyclic voltammetry (CV) tests were conducted from -0.4 to 0 V (vs. RHE) in N<sub>2</sub>-saturated 0.5 M H<sub>2</sub>SO<sub>4</sub> or 1 M KOH solution with the scan rate of 100 mV s<sup>-1</sup> for 10 000 segments and the differences in the LSV curves before and after CVs were compared.

## 3. Results and discussion

### 3.1 Physical characterization

SEM was used to observe the morphologies of the samples before carbonization. As shown in Fig. 1a and b, the Fe<sup>2+</sup>Ni-PBA has irregular aggregation while the Fe<sup>3+</sup>Ni-PBA is made of independent cubic nanocrystals. The addition of ammonium molybdate tetrahydrate made the Fe<sup>2+</sup>Ni-PBA particles stick together (Fig. 1c) while most of the Fe<sup>3+</sup>Ni-PBA cubes remained

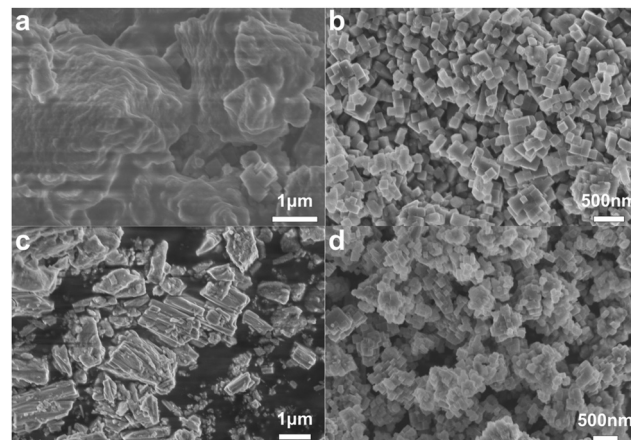


Fig. 1 SEM images of Fe<sup>2+</sup>Ni-PBA (a), Fe<sup>3+</sup>Ni-PBA (b), Fe<sup>2+</sup>NiMo (c), and Fe<sup>3+</sup>NiMo (d) before carbonization.



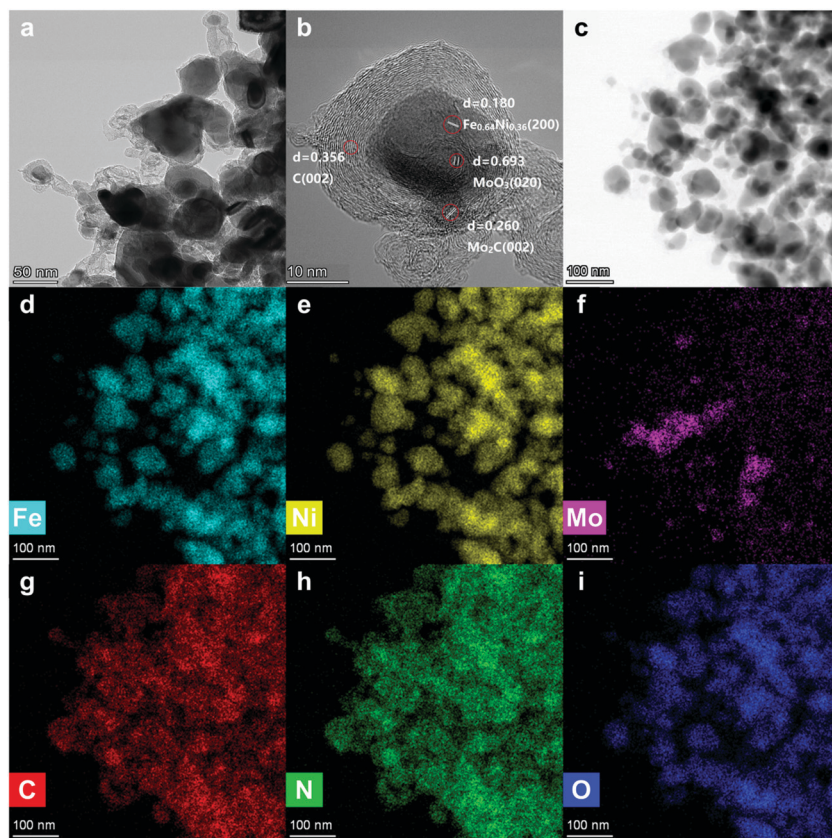


Fig. 2 TEM images (a–c) and the corresponding mapping images (d–i) of  $\text{Fe}^{3+}\text{NiMoC}$ .

uniform and independent after mixing (Fig. 1d), which allowed them to form dispersive nanoparticles after carbonization (Fig. 2a), thus enlarging the surface area and increasing the number of active sites.

In Fig. 2a, the metallic nanoparticles are surrounded by graphitic layers that can serve as a “cage”, encapsulating the metallic compounds inside. These carbon cages are connected by carbonized tubes made from N-doped carbon (Fig. 2g and h).

In order to investigate the morphology of the single carbon cage, high-resolution TEM was carried out. In Fig. 2b, the Fe, Ni and Mo compounds, including  $\text{Fe}_{0.64}\text{Ni}_{0.36}$ ,  $\text{Mo}_2\text{C}$  and  $\text{MoO}_3$ , are wrapped by the graphitic layers. The graphitic layers can serve as a carbon cage and encapsulate the Fe, Ni and Mo compounds inside, which can protect the active sites from the environment. The graphitic layers can also serve as a desirable electron transport medium due to its excellent conductivity. Thus, the graphitic layer structure can enhance the durability and improve the catalytic efficiency at the same time. Besides, the graphitic layers were not oriented parallel to the axis and showed considerable defects and edges on the surface,<sup>31</sup> which can improve the surface affinity for  $\text{H}^+$  in the solution.

The XRD pattern of  $\text{Fe}^{3+}\text{NiMoC}$  is shown in Fig. 3a. The typical peak at  $\approx 25^\circ$  indicates the (002) face of graphite carbon, which is characteristic of the carbon framework. The diffraction peaks at  $43.6^\circ$ ,  $50.8^\circ$ , and  $74.7^\circ$  can be indexed to the (111), (200), and (220) planes of  $\text{Fe}_{0.64}\text{Ni}_{0.36}$ , and the peaks at  $34.3^\circ$ ,  $37.9^\circ$ ,  $39.3^\circ$ ,  $52.1^\circ$ ,  $61.4^\circ$ ,  $69.5^\circ$ ,  $72.3^\circ$ ,  $74.5^\circ$  and  $75.5^\circ$  can be

assigned to the (021), (200), (121), (221), (040), (321), (042), (240) and (142) planes of  $\text{Mo}_2\text{C}$ .<sup>32</sup>

In order to investigate the compound surface including the chemical composition and element bonding configurations, X-ray photoelectron spectroscopy (XPS) was carried out for  $\text{Fe}^{3+}\text{NiMoC}$ . As shown in Fig. 3b, the existence of C, N, O, Fe, Ni and Mo with the atomic contents of C-43.15%, N-22.47%, O-20.15%, Fe-3.75%, N-2.16% and Mo-8.32% was confirmed. In the C 1s spectra (Fig. 3c), the peaks were observed at 284.5, 285.5, and 286.5 eV, which can be ascribed to C=C, C-C and C-O, respectively.<sup>33,34</sup> Fig. 3d shows the high-resolution spectrum of N 1s, which presents 4 types of N coordination environments at 398.6 eV for pyridinic-N, 400.3 eV for pyrrolic-N, 401.1 eV for graphitic-N and 402.7 eV for oxidized-N.<sup>35,36</sup> Meanwhile, the N content was determined to be 3.94 at%, which suggests that N atoms have been successfully doped into the carbon network. N doping in the porous carbon is beneficial for stabilizing metallic Fe, Ni and Mo as well as their compounds. In the meantime, it can regulate the electronic structure and surface permeability of catalyst.<sup>5</sup> The O 1s spectrum in Fig. 3e contains three peaks at 530.4 eV, 531.0 eV and 532.1 eV belonging to lattice oxygen, -OH groups and adsorbed  $\text{H}_2\text{O}$ , respectively. These three peaks all shifted to high binding energies compared to pure  $\text{MoO}_3$ ,<sup>37</sup> suggesting that electrons were transferred from the oxygen of  $\text{MoO}_3$  to Ni, which decreased the electron cloud density of oxygen. Therefore, the binding energies changed and partial oxygen vacancies were



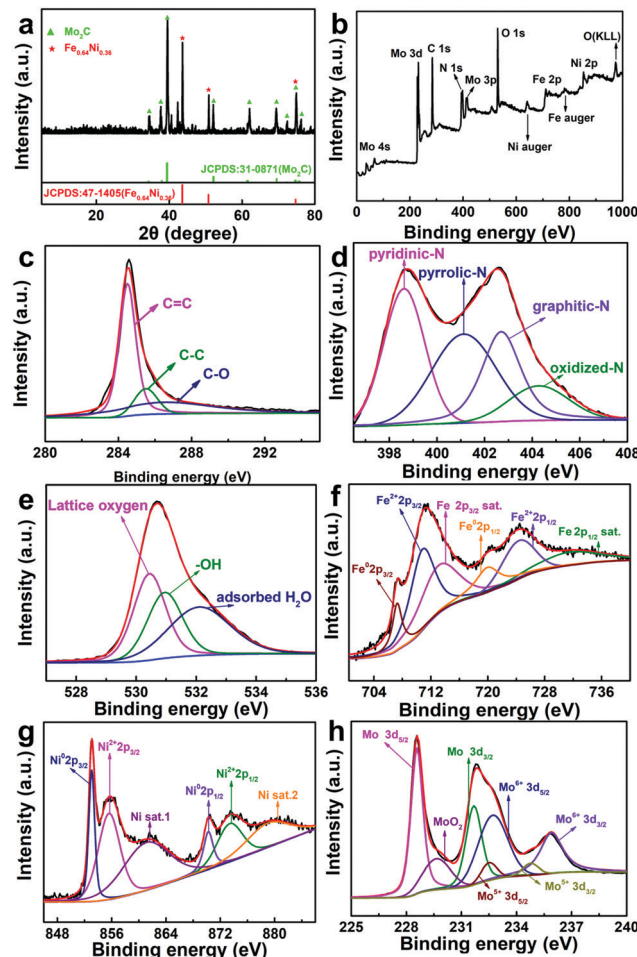


Fig. 3 XRD pattern (a), XPS survey spectrum (b) and the corresponding high-resolution spectra (c–h) of  $\text{Fe}^{3+}\text{NiMoC}$ .

formed.<sup>38,39</sup> In Fig. 3f and g, the  $\text{Fe}^{0+2p}$  and  $\text{Ni}^{0+2p}$  peaks can be ascribed to the  $\text{Fe}^{3+}$  and  $\text{Ni}^{2+}$  ions being reduced to  $\text{Fe}_{0.64}\text{Ni}_{0.36}$  at high temperature. The  $\text{Fe}^{2+2p}$  and  $\text{Ni}^{2+2p}$  peaks may belong to the coordination center of N-doped carbon. In addition, the Fe and Ni satellite peaks can be ascribed to the formation of the iron carbide and the spinel structure  $\text{NiFe}_2\text{O}_4$ ,<sup>40,41</sup> which were possibly produced by calcining the  $\text{Fe}^{3+}$ ,  $\text{Ni}^{2+}$  and sodium citrate at high temperatures and both have been reported to be excellent active centres toward the HER.<sup>31</sup> In Fig. 3h, the Mo 3d peaks at 232.7 eV and 235.8 eV are assigned to  $\text{Mo}^{6+}3d_{5/2}$  and  $\text{Mo}^{6+}3d_{3/2}$  of  $\text{MoO}_3$  produced by the thermal decomposition of ammonium molybdate.<sup>42</sup>  $\text{Mo}^{5+}$  peaks (232.5 eV and 234.8 eV) reveal the formation of oxygen vacancies due to the substitution of Ni and Fe atoms for Mo atoms in  $\text{MoO}_3$  lattice.<sup>43</sup>

In the XRD patterns,  $\text{Mo}_2\text{C}$  has the highest content among the Mo compounds while XPS indicates that the oxide of Mo dominates. This is mostly because XRD studies the bulk phase while XPS focuses on the surface; *i.e.*,  $\text{Fe}^{3+}\text{NiMoC}$  is mainly made up of  $\text{Fe}_{0.64}\text{Ni}_{0.36}$  and  $\text{Mo}_2\text{C}$  with the surface oxidation of Mo. In general, the N-doped carbon network established by carbonizing  $\text{Fe}^{3+}\text{Ni-PBA}$  can serve as a conductive fundamental base to tightly immobilize carbon cages. The carbon cages can

form a natural barrier to keep metallic active sites inside from being damaged by the environment. The low oxygen coordinated defect sites in the Fe, Ni and Mo compounds can serve as the HER active center, thus enhancing the electrocatalytic activity.<sup>30,44,45</sup>

### 3.2 HER catalytic activities in acidic solution

The HER catalytic performance was firstly tested in 0.5 M  $\text{H}_2\text{SO}_4$ . As seen in Fig. 4a and b,  $\text{Fe}^{3+}\text{Ni-PBAC}$  (471 mV *vs.* RHE) and  $\text{Fe}^{3+}\text{NiMoC}$  (246 mV *vs.* RHE) showed lower overpotentials as compared to  $\text{Fe}^{2+}\text{Ni-PBAC}$  (616 mV *vs.* RHE) and  $\text{Fe}^{2+}\text{NiMoC}$  (393 mV *vs.* RHE) at 10 mA  $\text{cm}^{-2}$ , respectively, which suggests that the electrocatalysts synthesized by  $\text{Fe}^{3+}$  have better catalytic activity toward the HER. This is probably due to the uniform and independent catalytic units providing a larger surface area and more active sites. On the other hand,  $\text{Fe}^{2+}\text{NiMoC}$  and  $\text{Fe}^{3+}\text{NiMoC}$  showed lower overpotentials (393 mV and 246 mV *vs.* RHE) compared to the  $\text{Fe}^{2+}\text{Ni-PBAC}$  and  $\text{Fe}^{3+}\text{Ni-PBAC}$  (616 mV and 417 mV *vs.* RHE) at 10 mA  $\text{cm}^{-2}$ , respectively, which indicates that the addition of Mo and its compounds can enhance the catalytic efficiency toward the HER. This is consistent with the results of a previous report.<sup>46</sup> For comparison, the 20% Pt/C was tested in the same way and showed an overpotential of 42 mV (*vs.* RHE) (Fig. 3a).

To gain insight into the kinetics and mechanism for the HER, the Tafel plots derived from the corresponding polarization curves are presented in Fig. 4c. The  $\text{Fe}^{3+}\text{NiMoC}$  displays a Tafel slope of  $-75.1$  mV  $\text{dec}^{-1}$  compared to Pt/C catalyst ( $-33.0$  mV  $\text{dec}^{-1}$ ). The Tafel slope is an intrinsic property of the electrocatalytic HER activity, which is related to the rate-determining step of the HER. A lower Tafel slope shows better HER kinetics.<sup>47</sup> In the aqueous electrolyte,  $\text{H}^+$  ions obtained electrons to form H atoms and were adsorbed on the surface of the working electrode (Volmer reaction,  $\text{H}_3\text{O}^+ + \text{e}^- \rightarrow \text{H}_{\text{ads}}$ ),<sup>48</sup> followed by either an electrochemical desorption step (Heyrovsky reaction,  $\text{H}_{\text{ads}} + \text{H}_3\text{O}^+ + \text{e}^- \rightarrow \text{H}_2$ ) or a chemical

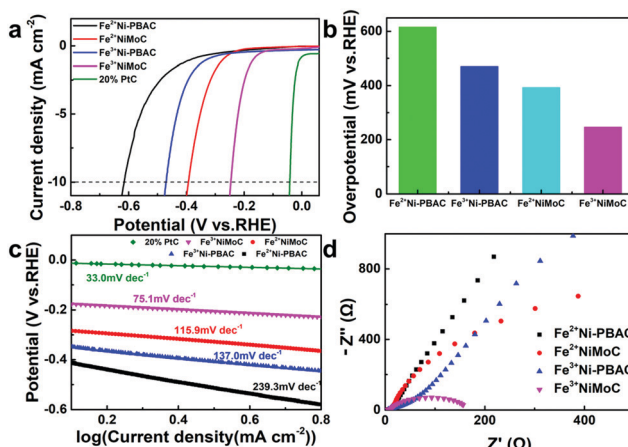


Fig. 4 (a) iR-corrected LSV curves of  $\text{Fe}^{2+}\text{Ni-PBAC}$ ,  $\text{Fe}^{3+}\text{Ni-PBAC}$ ,  $\text{Fe}^{2+}\text{NiMoC}$ ,  $\text{Fe}^{3+}\text{NiMoC}$  and 20% Pt/C; (b) the corresponding overpotentials at 10 mA  $\text{cm}^{-2}$ . (c) Tafel plots and (d) EIS spectra for the HER at  $-0.3$  V (*vs.* RHE). The electrolyte solution was 0.5 M  $\text{H}_2\text{SO}_4$ .

desorption step ( $H_{ads} + H_{ads} \rightarrow H_2$ ) to form hydrogen molecules.<sup>5</sup> The theoretical Tafel slopes of the Volmer, Heyrovsky and Tafel reactions are  $-120$ ,  $-40$  and  $-30$  mV dec $^{-1}$ , respectively. The Tafel slope of the  $Fe^{3+}NiMoC$  was  $-75.1$  mV dec $^{-1}$ , which is a Volmer–Heyrovsky mechanism with the Heyrovsky step is the rate-determining step.<sup>48</sup> In order to study the charge transfer resistances of these 4 samples, the electrochemical impedance spectra were employed. Fig. 4d is the EIS of  $Fe^{2+}Ni$ -PBAC,  $Fe^{3+}Ni$ -PBAC,  $Fe^{2+}NiMoC$  and  $Fe^{3+}NiMoC$  at  $-0.3$  V (vs. RHE). The  $Fe^{3+}NiMoC$  has the minimum charge transfer resistance and thus promotes the kinetics of the HER. Besides, the charge transfer resistances and Tafel slopes,  $Fe^{3+}NiMoC < Fe^{2+}NiMoC < Fe^{3+}Ni$ -PBAC  $< Fe^{2+}Ni$ -PBAC, which is consistent with the trend of the HER overpotentials mentioned above (Fig. 4a and b).

### 3.3 HER catalytic activities in alkaline solution

The HER catalytic performance was also tested in 1 M KOH. As shown in Fig. 5b and c,  $Fe^{3+}NiMoC$  exhibits the smallest Tafel slope and overpotential ( $116.9$  mV dec $^{-1}$ ,  $199$  mV) of all samples ( $Fe^{3+}Ni$ -PBAC( $133.1$  mV dec $^{-1}$ ,  $298$  mV),  $Fe^{2+}NiMoC$ ( $135.2$  mV dec $^{-1}$ ,  $355$  mV),  $Fe^{2+}Ni$ -PBAC( $209.7$  mV dec $^{-1}$ ,  $548$  mV)) except for the commercial Pt/C catalyst ( $54.2$  mV dec $^{-1}$ ,  $43$  mV), which suggests that the HER kinetics of  $Fe^{3+}NiMoC$  is favorable and the current density of  $Fe^{3+}NiMoC$  will increase faster as the potential becomes more negative. EIS spectra are also shown in Fig. 5d, illustrating that  $Fe^{3+}NiMoC$  has the smallest intrinsic resistance and charge transfer resistance, which facilitates the kinetics towards the HER, too.

It is worth noting that in alkaline solution (1 M KOH), the order of catalytic efficiency is as follows:  $Fe^{3+}NiMoC > Fe^{3+}Ni$ -PBAC  $> Fe^{2+}NiMoC > Fe^{2+}Ni$ -PBAC. However, in acidic solution (0.5 M  $H_2SO_4$ ), the order is  $Fe^{3+}NiMoC > Fe^{2+}NiMoC > Fe^{3+}Ni$ -PBAC  $> Fe^{2+}Ni$ -PBAC. In other words, the  $Fe^{3+}Ni$ -PBAC shows a better catalytic effect in alkaline solution while the  $Fe^{2+}NiMoC$  is better in the acidic solution.

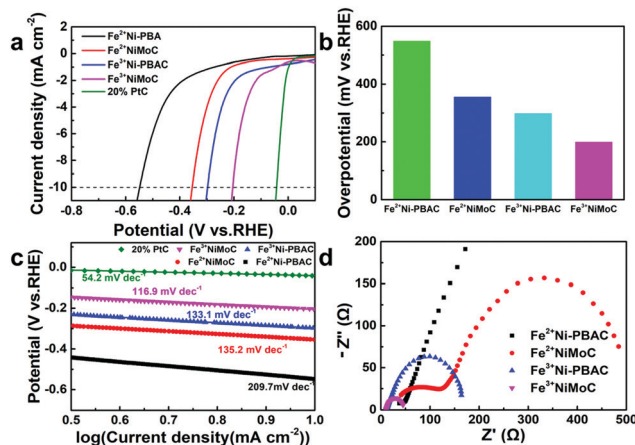


Fig. 5 iR-corrected LSV curves of  $Fe^{2+}Ni$ -PBAC,  $Fe^{3+}Ni$ -PBAC,  $Fe^{2+}NiMoC$ ,  $Fe^{3+}NiMoC$  and 20% Pt/C (a); the corresponding overpotentials at  $10$  mA cm $^{-2}$  (b); Tafel plots (c) and EIS spectra for HER at  $-0.3$  V (vs. RHE) (d). The electrolyte solution was 1 M KOH.

This is probably because in acidic solution, the desorption of  $H_2$  ( $H_{ads} + H_{ads} \rightarrow H_2$ ) is the rate-determining step due to the abundant  $H^+$  environment, and the  $Fe^{2+}NiMoC$  has a weaker adsorption capacity toward  $H_{ads}$  so it exhibits a better catalytic effect than  $Fe^{3+}Ni$ -PBAC. When it comes to the alkaline solution, the adsorption of  $H^+$  ( $H_3O^+ + e^- \rightarrow H_{ads}$ ) is the rate-determining step on account of the lack of  $H^+$ . Therefore, the independent catalytic units and larger surface area led to  $Fe^{3+}Ni$ -PBAC demonstrating preferable catalytic performance in alkaline solution.

### 3.4 Durability and activities of electrocatalyst

The ECSA was estimated by CVs with the equation  $ECSA = C_{dl}/C_s$  (where  $C_{dl}$  is the double layer capacitance,  $C_s$  is the capacitive behavior). The larger ECSA means more active sites.<sup>49</sup> Since the  $C_s$  of  $Fe^{3+}NiMoC$  is unknown, we can estimate the ECSA by comparing the value of  $C_{dl}$ ;  $C_{dl}$  can be calculated from the slope of the  $\Delta J$ -scan rate line.<sup>50</sup> The CV was firstly tested from  $-0.65$  to  $-0.55$  V (vs.  $Hg/Hg_2SO_4$ ) with scan rates from  $10$  to  $100$  mV s $^{-1}$  in 0.5 M  $H_2SO_4$  (Fig. 6a and b).  $C_{dl}$  was calculated with  $\Delta J = 0.60$  V (vs.  $Hg/Hg_2SO_4$ ). The value of  $C_{dl}$  ( $\mu$ F cm $^{-2}$ ) is half of the slope,<sup>51</sup> which is  $12.9$   $\mu$ F cm $^{-2}$  for  $Fe^{3+}NiMoC$ ,  $2.9$   $\mu$ F cm $^{-2}$  for  $Fe^{3+}Ni$ -PBAC,  $1.6$   $\mu$ F cm $^{-2}$  for  $Fe^{2+}NiMoC$  and  $0.5$   $\mu$ F cm $^{-2}$  for  $Fe^{2+}Ni$ -PBAC. The CV was also tested from  $-0.90$  to  $-0.80$  V (vs.  $Hg/HgO$ ) with a scan rate from  $10$  to  $100$  mV s $^{-1}$  in 1 M KOH (Fig. 6c and d).  $C_{dl}$  was calculated with  $\Delta J$  at  $-0.85$  V (vs.  $Hg/HgO$ ). The value of  $C_{dl}$  ( $\mu$ F cm $^{-2}$ ) was

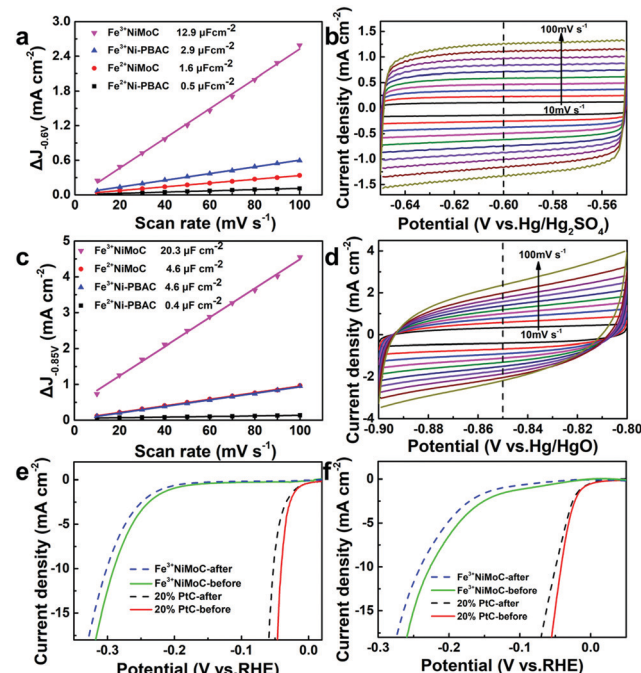


Fig. 6  $C_{dlS}$  was calculated with  $\Delta J$  at  $-0.60$  V (vs.  $Hg/Hg_2SO_4$ ) in 0.5 M  $H_2SO_4$  (a) and the corresponding CV curves of  $Fe^{3+}NiMoC$  (b).  $C_{dlS}$  was calculated with  $\Delta J$  at  $-0.85$  V (vs.  $Hg/HgO$ ) in 1 M KOH (c) and the corresponding CV curves of  $Fe^{3+}NiMoC$  (d). iR-corrected LSV curves of  $Fe^{3+}NiMoC$  and Pt/C before and after 10 000 CVs in 0.5 M  $H_2SO_4$  (e) and in 1 M KOH (f).



20.3  $\mu\text{F cm}^{-2}$  for  $\text{Fe}^{3+}\text{NiMoC}$ , 4.6  $\mu\text{F cm}^{-2}$  for  $\text{Fe}^{3+}\text{Ni-PBAC}$ , 4.6  $\mu\text{F cm}^{-2}$  for  $\text{Fe}^{2+}\text{NiMoC}$  and 0.4  $\mu\text{F cm}^{-2}$  for  $\text{Fe}^{2+}\text{Ni-PBAC}$ . It was assumed that the catalytic effect can be improved with the increasing quantity of catalytically active sites, which is consistent with the results of 3.2 and 3.3.

In order to investigate the durability of the catalyst, CVs were carried out in 0.5 M  $\text{H}_2\text{SO}_4$  or 1 M KOH solution.  $\text{Fe}^{3+}\text{NiMoC}$  and 20% commercial Pt/C were electrolyzed from -0.4 to 0 V (vs. RHE) in  $\text{N}_2$ -saturated 0.5 M  $\text{H}_2\text{SO}_4$  or 1 M KOH solution with the scan rate of 100 mV  $\text{s}^{-1}$  for 10 000 segments. In Fig. 6e and f, the LSV curves before and after CVs demonstrate that  $\text{Fe}^{3+}\text{NiMoC}$  has less current density loss after CVs than commercial 20% Pt/C in 0.5 M  $\text{H}_2\text{SO}_4$  or 1 M KOH, which suggests that  $\text{Fe}^{3+}\text{NiMoC}$  is more durable compared to commercial Pt/C.

## 4. Conclusion

In summary, we synthesized a new carbon cage-encapsulated FeNiMo compound material to electrocatalyze the HER. This non-noble metal catalyst exhibits excellent electrocatalytic performance in both acidic (246 mV, 10 mA  $\text{cm}^{-2}$ ) and alkaline (199 mV, 10 mA  $\text{cm}^{-2}$ ) solutions. More importantly, we have found a cheap and feasible way to establish a carbon cage structure, which can further enhance the durability of the non-metal catalyst. In general, this paper provides a promising way to decrease the cost of the catalyst for the HER by using an efficient and durable non-noble metal catalyst to replace the noble-metal one.

## Conflicts of interest

The authors have no competing interests to declare.

## Acknowledgements

This work was supported by National Key R&D Program of China (No. 2016YFC1102802).

## References

- P. Lu, Y. Yang, J. Yao, M. Wang, S. Dipazir, M. Yuan, J. Zhang, X. Wang, Z. Xie and G. Zhang, *Appl. Catal., B*, 2019, **241**, 113–119.
- W. Lubitz and W. Tumas, *Chem. Rev.*, 2007, **107**, 3900–3903.
- J. Zhang, W. Jia, S. Dang and Y. Cao, *J. Colloid Interface Sci.*, 2020, **560**, 161–168.
- Z. Tao, T. Wang, X. Wang, J. Zheng and X. Li, *ACS Appl. Mater. Interfaces*, 2016, **8**, 35390–35397.
- J. Huang, C. Du, J. Nie, H. Zhou, X. Zhang and J. Chen, *Electrochim. Acta*, 2019, **326**, 134982.
- J. Tian, Q. Liu, A. M. Asiri and X. Sun, *J. Am. Chem. Soc.*, 2014, **136**, 7587–7590.
- A. Kumar and S. Bhattacharyya, *ACS Appl. Mater. Interfaces*, 2017, **9**, 41906–41915.
- W. Zhu, R. Zhang, F. Qu, A. M. Asiri and X. Sun, *ChemCatChem*, 2017, **9**, 1721–1743.
- J. Wang, W. Cui, Q. Liu, Z. Xing, A. M. Asiri and X. Sun, *Adv. Mater.*, 2016, **28**, 215–230.
- T. Y. Ma, S. Dai, M. Jaroniec and S. Z. Qiao, *J. Am. Chem. Soc.*, 2014, **136**, 13925–13931.
- L. Zhang, I. S. Amiinu, X. Ren, Z. Liu, G. Du, A. M. Asiri, B. Zheng and X. Sun, *Inorg. Chem.*, 2017, **56**, 13651–13654.
- X. Ren, W. Wang, R. Ge, S. Hao, F. Qu, G. Du, A. M. Asiri, Q. Wei, L. Chen and X. Sun, *Chem. Commun.*, 2017, **53**, 9000–9003.
- W. Wang, L. Yang, F. Qu, Z. Liu, G. Du, A. M. Asiri, Y. Yao, L. Chen and X. Sun, *J. Mater. Chem. A*, 2017, **5**, 16585–16589.
- W. Wang, X. Ren, S. Hao, Z. Liu, F. Xie, Y. Yao, A. M. Asiri, L. Chen and X. Sun, *Chem. – Eur. J.*, 2017, **23**, 12718–12723.
- D.-H. Ha, B. Han, M. Risch, L. Giordano, K. P. C. Yao, P. Karayalali and Y. Shao-Horn, *Nano Energy*, 2016, **29**, 37–45.
- Y. Zhang, Y. Liu, M. Ma, X. Ren, Z. Liu, G. Du, A. M. Asiri and X. Sun, *Chem. Commun.*, 2017, **53**, 11048–11051.
- T. Liu, D. Liu, F. Qu, D. Wang, L. Zhang, R. Ge, S. Hao, Y. Ma, G. Du, A. M. Asiri, L. Chen and X. Sun, *Adv. Energy Mater.*, 2017, **7**, 1700020.
- T. Liu, L. Xie, J. Yang, R. Kong, G. Du, A. M. Asiri, X. Sun and L. Chen, *ChemElectroChem*, 2017, **4**, 1840–1845.
- L. Zhang, X. Ren, X. Guo, Z. Liu, A. M. Asiri, B. Li, L. Chen and X. Sun, *Inorg. Chem.*, 2018, **57**, 548–552.
- R. Zhang, X. Ren, S. Hao, R. Ge, Z. Liu, A. M. Asiri, L. Chen, Q. Zhang and X. Sun, *J. Mater. Chem. A*, 2018, **6**, 1985–1990.
- X. F. Lu, L. Yu, J. Zhang and X. W. Lou, *Adv. Mater.*, 2019, **31**, 1900699.
- N. Cheng, L. Ren, G. Casillas, S. Zhou, J. Zhuang, L. Wang, X. Xu, S. X. Dou and Y. Du, *Sustainable Energy Fuels*, 2019, **3**, 1757–1763.
- J. Landon, E. Demeter, N. İnoğlu, C. Keturakis, I. E. Wachs, R. Vasić, A. I. Frenkel and J. R. Kitchin, *ACS Catal.*, 2012, **2**, 1793–1801.
- Y. Xu, W. Tu, B. Zhang, S. Yin, Y. Huang, M. Kraft and R. Xu, *Adv. Mater.*, 2017, **29**, 1605957.
- X. F. Lu, L. Yu and X. W. Lou, *Sci. Adv.*, 2019, **5**, eaav6009.
- M. F. Kibria and M. S. Mridha, *Int. J. Hydrogen Energy*, 1996, **21**, 179–182.
- M. Gong, Y. Li, H. Wang, Y. Liang, J. Z. Wu, J. Zhou, J. Wang, T. Regier, F. Wei and H. Dai, *J. Am. Chem. Soc.*, 2013, **135**, 8452–8455.
- J. Du, C. Chen, F. Cheng and J. Chen, *Inorg. Chem.*, 2015, **54**, 5467–5474.
- A. Subramania, A. R. Sathiya Priya and V. S. Muralidharan, *Int. J. Hydrogen Energy*, 2007, **32**, 2843–2847.
- X.-Y. Yu, Y. Feng, Y. Jeon, B. Guan, X. W. Lou and U. Paik, *Adv. Mater.*, 2016, **28**, 9006–9011.
- X. Zhao, P. Pachfule, S. Li, J. R. J. Simke, J. Schmidt and A. Thomas, *Angew. Chem., Int. Ed.*, 2018, **57**, 8921–8926.
- F.-X. Ma, H. B. Wu, B. Y. Xia, C.-Y. Xu and X. W. Lou, *Angew. Chem., Int. Ed.*, 2015, **54**, 15395–15399.



33 H. Zhang, S. Hwang, M. Wang, Z. Feng, S. Karakalos, L. Luo, Z. Qiao, X. Xie, C. Wang, D. Su, Y. Shao and G. Wu, *J. Am. Chem. Soc.*, 2017, **139**, 14143–14149.

34 J. Wang, D. Gao, G. Wang, S. Miao, H. Wu, J. Li and X. Bao, *J. Mater. Chem. A*, 2014, **2**, 20067–20074.

35 X. Fan, Z. Peng, R. Ye, H. Zhou and X. Guo, *ACS Nano*, 2015, **9**, 7407–7418.

36 Q. Qin, H. Jang, L. Chen, G. Nam, X. Liu and J. Cho, *Adv. Energy Mater.*, 2018, **8**, 1801478.

37 Y. Cao, H. Wang, R. Ding, L. Wang, Z. Liu and B. Lv, *Appl. Catal., A*, 2020, **589**, 117308.

38 L. Liu, N. Chen, Y. Lei, X. Xue, L. Li, J. Wang, S. Komarneni, H. Zhu and D. Yang, *J. Hazard. Mater.*, 2018, **360**, 279–287.

39 S. Bai, C. Chen, D. Zhang, R. Luo, D. Li, A. Chen and C.-C. Liu, *Sens. Actuators, B*, 2014, **204**, 754–762.

40 Q. Zhao, Z. Yan, C. Chen and J. Chen, *Chem. Rev.*, 2017, **117**, 10121–10211.

41 L. Cong, Z. Yu, F. Liu and W. Huang, *Catal. Sci. Technol.*, 2019, **9**, 1208–1214.

42 R. S. Mann and K. C. Khulbe, *Bull. Chem. Soc. Jpn.*, 1975, **48**, 1021–1023.

43 Z. Li, J. Ma, B. Zhang, C. Song and D. Wang, *CrystEngComm*, 2017, **19**, 1479–1485.

44 X.-F. Lu, L.-F. Gu, J.-W. Wang, J.-X. Wu, P.-Q. Liao and G.-R. Li, *Adv. Mater.*, 2017, **29**, 1604437.

45 H. Perron, T. Mellier, C. Domain, J. Roques, E. Simoni, R. Drot and H. Catalette, *J. Phys.: Condens. Matter*, 2007, **19**, 346219.

46 E. J. Sundstrom, X. Yang, V. S. Thoi, H. I. Karunadasa, C. J. Chang, J. R. Long and M. Head-Gordon, *J. Am. Chem. Soc.*, 2012, **134**, 5233–5242.

47 J. Wang, F. Xu, H. Jin, Y. Chen and Y. Wang, *Adv. Mater.*, 2017, **29**, 1605838.

48 H. Gao, J. Zang, X. Liu, Y. Wang, P. Tian, S. Zhou, S. Song, P. Chen and W. Li, *Appl. Surf. Sci.*, 2019, **494**, 101–110.

49 Q. Zhang, H. Zhong, F. Meng, D. Bao, X. Zhang and X. Wei, *Nano Res.*, 2018, **11**, 1294–1300.

50 Y. Yang, Z. Lun, G. Xia, F. Zheng, M. He and Q. Chen, *Energy Environ. Sci.*, 2015, **8**, 3563–3571.

51 M. A. Lukowski, A. S. Daniel, F. Meng, A. Forticaux, L. Li and S. Jin, *J. Am. Chem. Soc.*, 2013, **135**, 10274–10277.

